

1 Constructing “Li-rich Ni-rich” oxide cathodes for high-energy-density Li-ion 2 batteries

3 Biao Li^{1,2}, Gwenaëlle Rousse^{1,2,3}, Leiting Zhang⁴, Maxim Avdeev^{5,6}, Michaël Deschamps^{2,7}, Artem M.
4 Abakumov⁸, Jean-Marie Tarascon^{1,2,3*}

5 ¹Chimie du Solide-Energie, UMR 8260, Collège de France, 75231 Paris Cedex 05, France.

6 ²Réseau sur le Stockage Electrochimique de l’Energie (RS2E), FR CNRS 3459, France.

7 ³Sorbonne Université, 4 Place Jussieu, 75005, Paris, France.

8 ⁴Battery Electrodes and Cells, Electrochemistry Laboratory, Paul Scherrer Institute, Forschungsstrasse 111, 5232
9 Villigen-PSI, Switzerland. (*Present address: Department of Chemistry – Ångström Laboratory, Uppsala University,*
10 *Box 538, SE-751 21 Uppsala, Sweden.*)

11 ⁵School of Chemistry, The University of Sydney, Sydney, New South Wales, Australia.

12 ⁶Australian Centre for Neutron Scattering, Australian Nuclear Science and Technology Organisation, Kirrawee DC,
13 New South Wales, Australia.

14 ⁷CNRS, CEMHTI UPR3079, Université d’Orléans, Orléans, France

15 ⁸Center for Energy Science and Technology, Skolkovo Institute of Science and Technology, Nobel str. 3, 121205
16 Moscow, Russia.

17 * Corresponding author: jean-marie.tarascon@college-de-france.fr

18 **Key words:** Li-ion batteries, Li-rich, Ni-rich, layered, disordered

19

20 Abstract

21 The current exploration of high-energy-density cathode materials for Li-ion batteries is mainly
22 concentrated on either so-called “Li-rich” or “Ni-rich” oxides. However, both are suffering from
23 formidable practical challenges. Here, we combine these two concepts to obtain “Li-rich Ni-rich”
24 oxides in pursuit of more practical high-energy-density cathodes. As a proof of concept, we
25 synthesized an array of $\text{Li}_{1+y}\text{Ni}_{(3-5y)/3}\text{Mo}_{2y/3}\text{O}_2$ oxides, whose structures were identified to be the
26 coexistence of LiNiO_2 -rich and Li_4MoO_5 -rich domains with the aid of XRD, TEM, and NMR
27 techniques. Such intergrowth structure with 5-20 nm in size enables excellent mechanical and
28 structural reversibility for the layered rock-salt LiNiO_2 -rich domain upon cycling thanks to the
29 robust cubic rock-salt Li_4MoO_5 -rich domain enabling an “epitaxial stabilization” effect. As a result,
30 we achieved high capacities ($>220 \text{ mA h g}^{-1}$) with Ni contents as low as 80%; the
31 $\text{Li}_{1.09}\text{Ni}_{0.85}\text{Mo}_{0.06}\text{O}_2$ member ($y = 0.09$) shows much improved cycling performances (91%
32 capacity retention for 100 cycles at C/10) compared with pure LiNiO_2 . This work validates the
33 feasibility of constructing Li-rich Ni-rich compounds in a form of intergrowing domains and hence
34 unlocks vast possibilities for future cathode design.

35

36 Introduction

37 The electric vehicles (EVs) market is under rapid growth, as witnessed by the number of
38 EVs on the roads that has set a new record (>10 millions) at the end of 2020¹. The prosperity of
39 the EV market is driving the demand for high-energy-density Li-ion batteries acting as power
40 sources. Throughout the past decades, enormous efforts have been devoted to exploring potential
41 candidates for both cathodes and anodes in pursuit of higher energy densities. Among them,
42 classical cathode candidates, such as LiCoO_2 , LiFePO_4 , and $\text{LiNi}_{1/3}\text{Co}_{1/3}\text{Mn}_{1/3}\text{O}_2$, primarily suffer
43 from low capacities, typically below 200 mA h g^{-1} and, therefore, low energy densities.² Hence,
44 practical high-energy-density electrodes are pressingly demanded.

45 The current exploration of high-energy-density cathode materials is ongoing along two
46 routes. The first concerns the so-called Li-rich materials, $\text{Li}_{1+x}\text{M}_{1-x}\text{O}_2$ (M denotes transition metal
47 hereafter), with additional Li ions partially replacing M ions at the transition metal layer.³ They
48 can provide exceptionally high capacities ($>250 \text{ mA h g}^{-1}$) stemming from anionic redox
49 phenomenon, a paradigm-shift concept that is receiving worldwide attentions⁴⁻⁷. However, this
50 class of materials are plagued by their common shortcomings such as voltage hysteresis and
51 voltage fade brought forward by the aforementioned anionic redox, and their prospect of practical
52 use remains unclear unless these bottlenecks are overcome^{4,8}.

53 In parallel, the community is also striving on another strategy — the so-called Ni-rich (or
54 high-Ni) oxides with either the $\text{LiNi}_x\text{Co}_y\text{Mn}_{1-x-y}\text{O}_2$ (NMC) or $\text{LiNi}_x\text{Co}_y\text{Al}_{1-x-y}\text{O}_2$ (NCA)
55 compositions with x typically equal or larger than 0.8.^{9,10} They are derived from LiNiO_2 and are
56 generating great interest owing to their high capacities ($> 200 \text{ mA h g}^{-1}$) and high working
57 potentials ($\sim 3.8 \text{ V}$). However, these Ni-rich electrodes are suffering from mechanical,
58 electrochemical and thermal stability issues that, in some extent, limit their commercial use.¹¹
59 Therefore, our society is in dire need of new strategies for circumventing such weaknesses while
60 keeping or even increasing the cathode capacity.

61 In this work, we aim to explore the feasibility of merging the Li-rich concept into the Ni-
62 rich oxide materials as a potential solution of the dilemma mentioned above. This idea was initiated
63 by the fact that placing additional Li ions in Ni layer should create O 2p non-bonding states that
64 can serve as an additional redox reservoir, which can buffer the electron depletion from σ -type
65 $\text{Ni}(3d)\text{-O}(2p)$ hybridized states that was supposed to cause the devastation of oxygen framework.¹²⁻

66 ¹⁴ Besides, the replacement of Ni by Li will also increase the theoretical capacity and reduce the

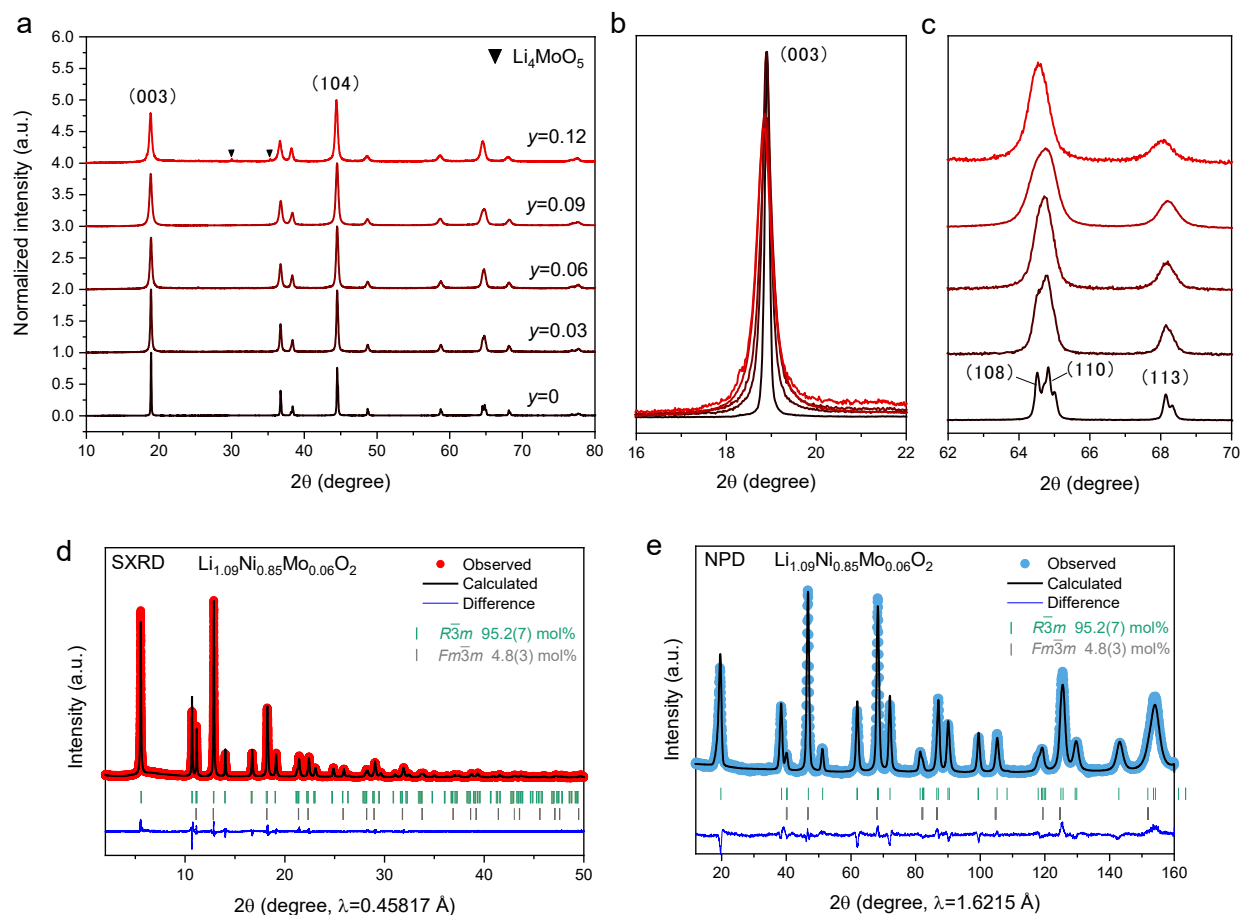
67 Ni content in order to get rid of the stability issues. As Li^+ is less positively charged than Ni^{3+} ,
68 such design strategy implies the need to introduce another high-valence metal ion, such as Mo^{6+} ,
69 W^{6+} , Nb^{5+} , and Mn^{4+} , to balance the charge. The introduction of these redox inactive metal ions
70 can also benefit the stabilization of the structure, as frequently suggested by previous works¹⁵⁻¹⁷.

71 We herein implement this strategy by placing additional Li^+ and Mo^{6+} ions, as a proof of
72 concept, into LiNiO_2 , to generate an array of Li-rich Ni-rich materials that can be nominally
73 formulated as $\text{Li}_{1+y}\text{Ni}_{(3-5y)/3}\text{Mo}_{2y/3}\text{O}_2$ ($y=0.03, 0.06, 0.09, \text{ and } 0.12$). We found that these materials,
74 instead of forming solid solutions, are composed of layered LiNiO_2 -based domains and Li_4MoO_5 -
75 based disordered rock-salt domains intergrown together, as evidenced by synchrotron X-ray
76 powder diffraction (SXRD), neutron powder diffraction (NPD), transmission electron microscopy
77 (TEM) and nuclear magnetic resonance (NMR) studies. As a result, these Li-rich Ni-rich
78 composites show comparable and even higher capacities ($210\sim 230 \text{ mA h g}^{-1}$), even with Ni
79 contents as low as 80%, compared with that of pure LiNiO_2 (220 mA h g^{-1}), with some of them
80 showing excellent cycling stabilities as well.

81

82 **Results and discussions**

83 **General structural characterizations.** $\text{Li}_{1+y}\text{Ni}_{(3-5y)/3}\text{Mo}_{2y/3}\text{O}_2$ ($y=0.03, 0.06, 0.09, \text{ and}$
84 0.12) were synthesized via a solution-preceded solid-state process (the details can be found in the
85 experimental section). The elemental compositions were checked by inductively coupled plasma
86 atomic emission spectroscopy (ICP-AES), showing Li/Ni ratios consistent with the nominal ones
87 (Table S1). However, Mo contents were found to be far below the theoretical values, which is due
88 to the Mo oxides (e.g. MoO_3) have limited solubility in acidic media especially when aqua regia
89 was used for ICP-AES measurements¹⁸. Scanning electron microscopy (SEM) coupled with
90 energy dispersive X-ray analysis (EDX) was further employed to validate the Ni/Mo ratios, as
91 tabulated in Table S2, showing good consistency with the nominal values.

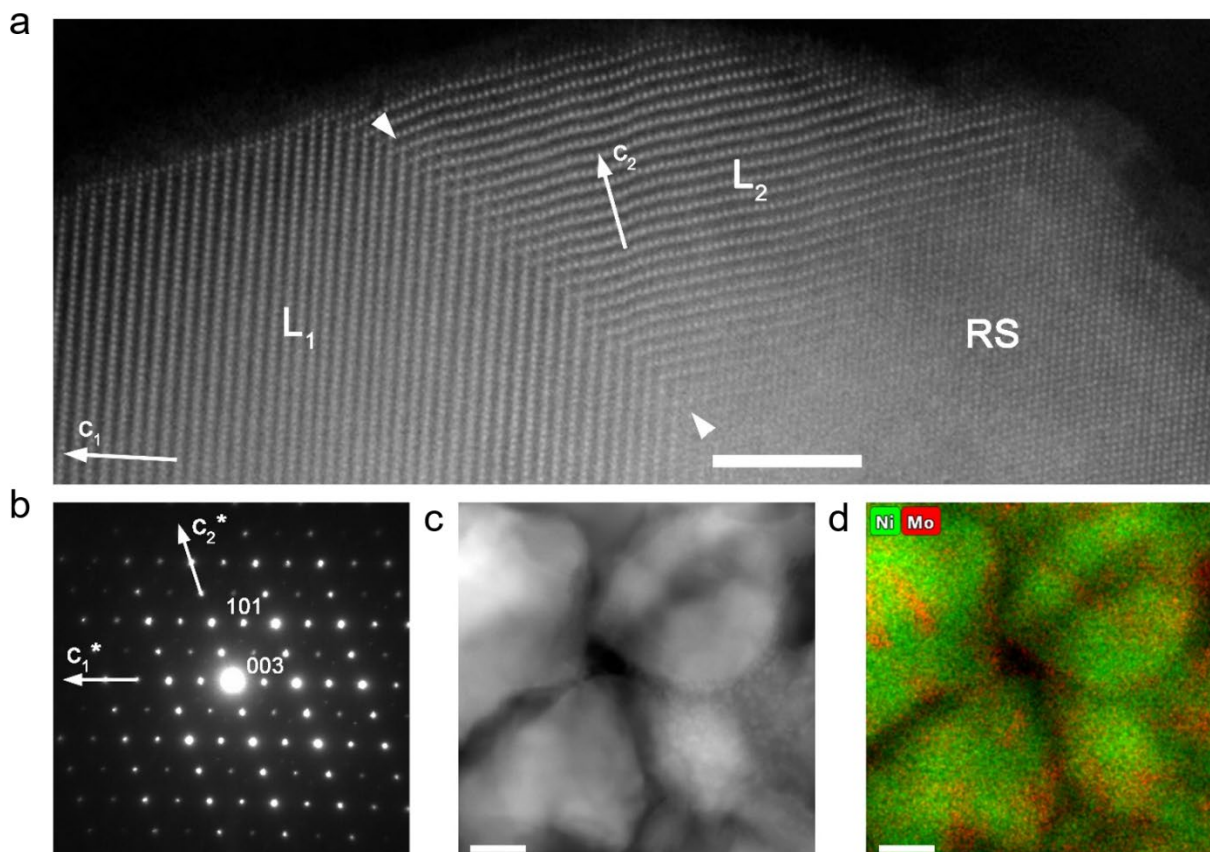


92

93 **Figure 1. Structural characterizations of $\text{Li}_{1+y}\text{Ni}_{(3-5y)/3}\text{Mo}_{2y/3}\text{O}_2$ ($y=0, 0.03, 0.06, 0.09, 0.12$).** (a) XRD
 94 patterns. (b)(c) Enlarged parts of XRD patterns. (d)(e) Combined Rietveld refinement results of SXR D and
 95 NPD for the $y=0.09$ member ($\text{Li}_{1.09}\text{Ni}_{0.85}\text{Mo}_{0.06}\text{O}_2$). The refinement was done with a two-phase model with
 96 $\text{Li}_{1.04}\text{Ni}_{0.93}\text{Mo}_{0.03}\text{O}_2$ ($R\bar{3}m$) and Li_4MoO_5 ($Fm\bar{3}m$) whose molar percentage was indicated. The color-coded
 97 vertical bars are the Bragg positions of each phase.

98 X-ray powder diffraction (XRD) was further employed to investigate the structures of the
 99 as-synthesized $\text{Li}_{1+y}\text{Ni}_{(3-5y)/3}\text{Mo}_{2y/3}\text{O}_2$ samples. As shown in Fig. 1a, LiNiO_2 is well crystallized in
 100 a typical layered structure with $R\bar{3}m$ symmetry in line with what has been reported previously¹⁹.
 101 Upon the addition of Li and Mo, the diffraction peaks are getting broader as observed from the
 102 evolution of (003) peak (Fig. 1b) and (108), (110) peaks (Fig. 1c). This indicates a decrease of the
 103 crystallite sizes, as identified by the SEM images (Fig. S1), with probably also an increasing degree
 104 of the micro-strain. Besides, the lattice parameter a and c , obtained via Rietveld refinement,
 105 generally increase as a function of Li content (Fig. S2). Such lattice expansion suggests the
 106 successful incorporation into the LiNiO_2 lattice of additional Li^+ ions, the ionic radius of which
 107 ($\sim 0.76\text{\AA}$) is larger than that of Ni^{3+} ($\sim 0.56\text{\AA}$). In addition, the most prominent change is observed

108 for the (003) peak intensity, which gradually decreases relative to that of the (104) peak upon Li
 109 and Mo addition (Fig. 1a). Considering that the (003)/(104) peak intensity ratio is widely used to
 110 gauge the degree of cation mixing between the Li and M layers, we presumed that its decrease is
 111 a signature of the higher degree of cation mixing occurring upon Li and Mo incorporation.



112
 113 **Figure 2. TEM analysis of $\text{Li}_{1.09}\text{Ni}_{0.85}\text{Mo}_{0.06}\text{O}_2$.** (a) HAADF-STEM image showing the twinned domains
 114 of the layered $R\text{-}3m$ structure (L_1 and L_2) along with a disordered rock-salt (RS) domain. The orientation of
 115 the c -axis in the layered domains is marked with arrows. The (104) twin plane is traced with arrowheads.
 116 The scale bar is 5 nm. (b) ED pattern demonstrating the twinned layered O3-type structure. The reciprocal
 117 lattice axes c^* for the twinned domains are marked. (c) HAADF-STEM image and (d) the color-coded EDX
 118 map demonstrating the mosaic Ni (green) and Mo (red) distribution. The scale bar is 20 nm.

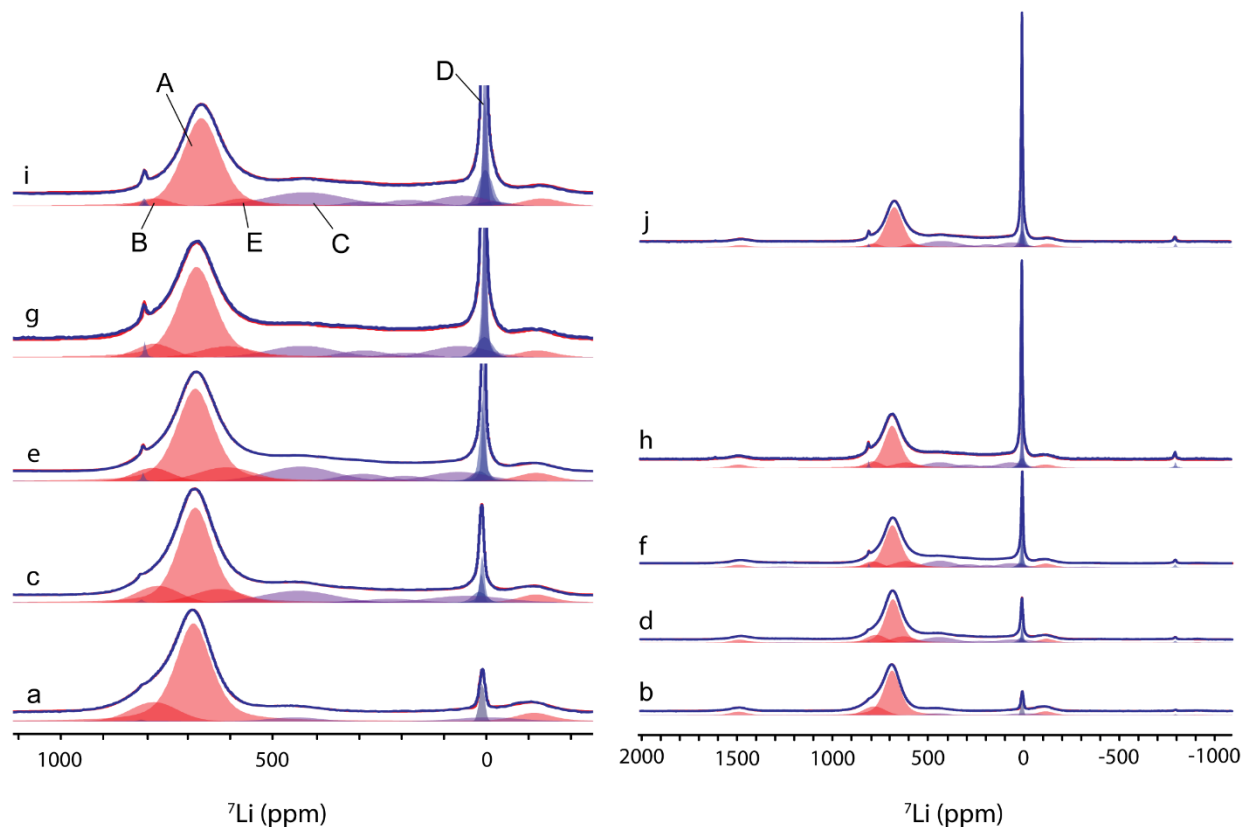
119 **TEM analysis.** Surprisingly, TEM images of the $\text{Li}_{1.09}\text{Ni}_{0.85}\text{Mo}_{0.06}\text{O}_2$ sample showed a
 120 two-phase intergrowth system rather than a solid solution. As shown in Fig. 2a,b, the high-angle
 121 annular dark-field scanning transmission electron microscopy (HAADF-STEM) image and
 122 electron diffraction (ED) pattern reveal that the O3 structure is split into twinned nanodomains
 123 separated by twin planes (marked with arrowheads in Fig. 2a; the detailed indexing of the ED
 124 pattern is provided in Fig.S3). The transition metals and Li cations in these domains are well

125 ordered as no HAADF intensity is observed between the brightest dots of the M columns. This
126 indicates low fractions of Ni and Mo in the octahedral Li sites. The apparent cationic disorder in
127 these domains is observed in the very surface layer (i.e. the thickness of one unit cell). However,
128 next to the well-ordered layered structure, rock-salt-type disordered domains were also found,
129 displaying a mixed distribution of the M and Li cations (marked as RS in Fig. 2a). Such a structural
130 inhomogeneity apparently coexists with a chemical inhomogeneity as unequivocally observed
131 from the energy dispersive X-ray (EDX) elemental mapping (Fig. 2c,d). It clearly shows a mosaic-
132 like Mo and Ni distribution pointing toward the coexistence of a Ni-rich phase and a Mo-rich phase.
133 The Ni:Mo atomic ratio quantified with the EDX spectra integrated over large areas (c.a. 200×200
134 nm) amounts to 93.3(6):6.7(6) that corresponds to $y = 0.09$, in agreement with the bulk
135 composition of the sample determined from ICP. The Ni:Mo = 97.2(5):2.8(5) atomic ratio was
136 measured for the Ni-rich phase that corresponds to $y = 0.04$ and hence a composition close to
137 $\text{Li}_{1.04}\text{Ni}_{0.93}\text{Mo}_{0.03}\text{O}_2$. The domains of the Mo-rich phase are too small and overlap heavily with the
138 Ni-rich phase, so their composition cannot be reliably determined.

139
140 **NMR analysis.** To explore the exact chemical structure of these intergrown phases, ^7Li NMR
141 spectroscopy was also used as it is an excellent probe of the paramagnetic ions around lithium
142 spins, providing access to their oxidation state and their connectivity to the observed lithium spin.

143 For typical Ni-based layered oxides, several Li environments can be distinguished by ^7Li
144 NMR depending on the number and position of Ni ions interacting through Ni-O-Li bonds. As
145 calculated in a lithium nickel cobalt oxide, each Ni^{3+} is expected to contribute to the ^7Li shift by
146 adding -15 ppm in an edge-sharing position (Li-O-Ni angle at 90°), and +110 ppm in a corner
147 sharing position (Li-O-Ni angle of 180°).²⁰⁻²² Those values are found to be -30 and +170 ppm for
148 Ni^{2+} .²³ Diamagnetic ions, such as Li^+ , Mo^{6+} ($4d^0$ ion) and Co^{4+} ($3d^6$ low-spin) are expected to
149 induce minor shift changes. These contributions would give rise to a shift of 570 ppm for a typical
150 layered LiNiO_2 compound (6 Li^+ -O- Ni^{3+} at 90° and 6 Li^+ -O- Ni^{3+} at 180°). Nevertheless, in our
151 case, the main LiNiO_2 peak was found at around 680 ppm (peak A in Fig. 3a), a value close to
152 those previously measured^{22,24,25} but slightly larger than the calculated one. The discrepancy may
153 stem from the local distortion arising around the Ni ions (Jahn-Teller) which was absent from the
154 structure used for the calculations. By further deconvolution of the NMR spectra, we also found
155 an extra peak on the left-hand side of the LiNiO_2 contribution (760-780 ppm, peak B in Fig. 3) in

156 all the samples. This peak can be assigned to the presence of Ni^{2+} ions (as in $\text{Li}_{1-z}\text{Ni}_{1+z}\text{O}_2$), which
 157 usually gives rise to larger shifts, and was also detected in a previous publication²¹ in which ^6Li
 158 MAS NMR showed a similar shoulder appearing on the left-hand side of the main peak correlating
 159 with Ni^{2+} . Interestingly, this peak (B) decreases upon Mo^{6+} addition (Fig. 3), starting at 13.4% of
 160 the total for pristine LiNiO_2 , down to 4-5% for $y=0.09$ and $y=0.12$ members.



161
 162 **Figure 3.** ^7Li MAS-NMR spectra of (a)(b) pristine LiNiO_2 , (c)(d) $\text{Li}_{1.03}\text{Ni}_{0.95}\text{Mo}_{0.02}\text{O}_2$, (e)(f)
 163 $\text{Li}_{1.06}\text{Ni}_{0.9}\text{Mo}_{0.04}\text{O}_2$, (g)(h) $\text{Li}_{1.09}\text{Ni}_{0.85}\text{Mo}_{0.06}\text{O}_2$, and (i)(j) $\text{Li}_{1.12}\text{Ni}_{0.8}\text{Mo}_{0.08}\text{O}_2$. The NMR spectra on the left
 164 hand side show the center region of the spectrum and the diamagnetic contribution (in blue) around 0 ppm
 165 is truncated. The full spectra are shown on the right hand side to illustrate the relative contributions of the
 166 diamagnetic components. The detailed results of the fits are shown in the Table S8. Different species are
 167 labelled with A, B, C, D and E corresponding to the Li signal of LiNiO_2 -rich phase, Ni^{2+} species (like in
 168 $\text{Li}_{1-z}\text{Ni}_{1+z}\text{O}_2$), Ni-rich rock salt phase, diamagnetic Li_4MoO_5 -rich phase, and less Mo^{6+} surrounded Li species,
 169 respectively.

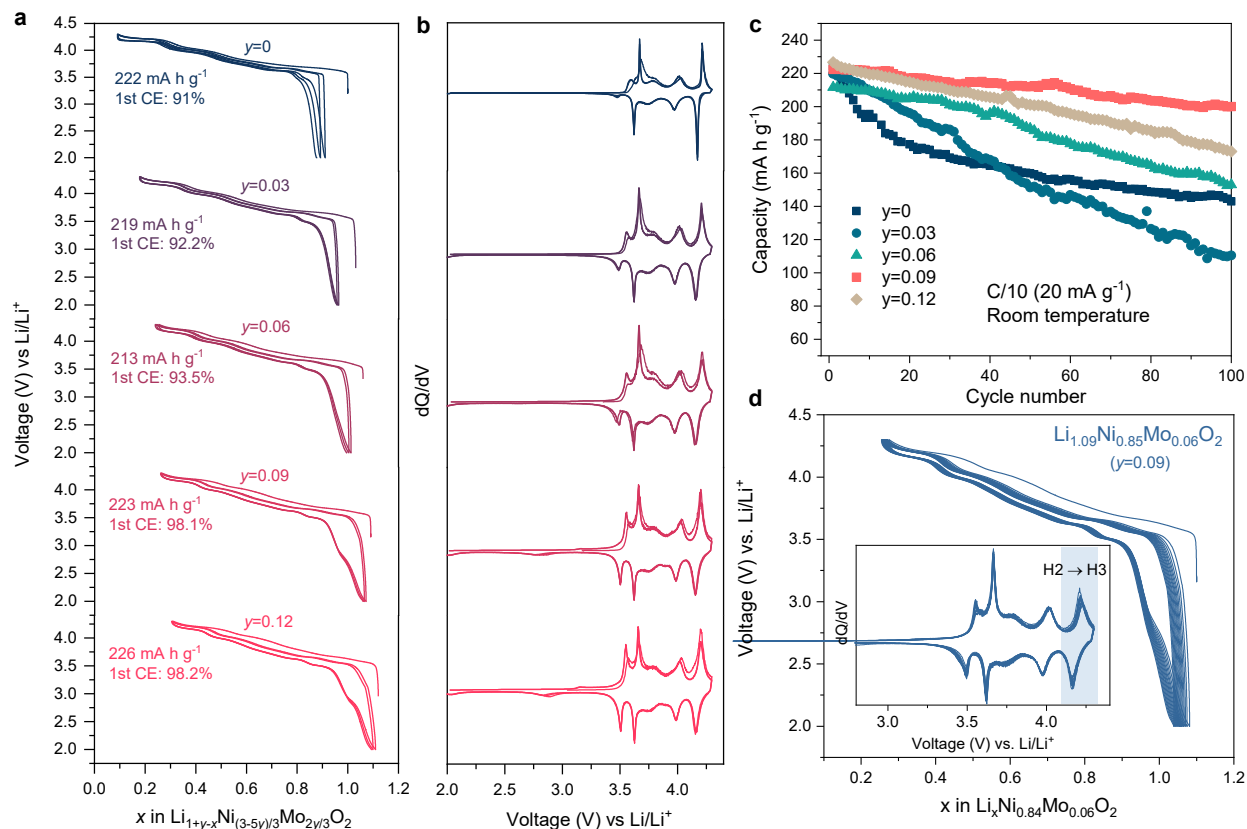
170 Mo^{6+} is a d^0 diamagnetic ion, and therefore, its contribution to the shift of neighboring ^7Li
 171 spins is expected to be negligible compared to Ni^{2+} and Ni^{3+} ions. The presence of a diamagnetic
 172 contribution (around 0 ppm, 7.9% of all lithium ions) in pristine LiNiO_2 usually stems from
 173 impurities originating from the synthesis process, i.e. lithium hydroxide or carbonate, as seen in
 174 numerous previous studies^{21,24,26}. On the other hand, an increasing diamagnetic contribution (peak

175 D around 0 ppm in Fig. 3) that is correlated with molybdenum concentration points towards the
176 creation of diamagnetic molybdenum and lithium-rich domains. This is confirmed by the ^7Li T_1 -
177 relaxation behavior of this diamagnetic part, which displays long T_1 constants (≈ 1 s) compared to
178 the T_1 of ^7Li in the paramagnetic phase (2-5 ms), indicating that those lithium ions are far away
179 from Ni^{2+} or Ni^{3+} ions. Considering the stoichiometry of the diamagnetic domains, one could
180 expect a Li/Mo ratio of 4 in this phase, pointing towards Li_4MoO_5 composition. In such a case, the
181 proportion of lithium belonging to this phase is expected to be 7.8%, 15.1%, 22.0% and 28.6% for
182 $y=0.03$, 0.06, 0.09 and 0.12 samples, respectively, in good consistency with experimental ones
183 (7.1%, 12.6%, 21.1%, and 24.1%) of the ^7Li spins that belong to the diamagnetic domains (Table
184 S7). The slightly less lithium than expected is not surprising, since we neglected the interface
185 between the two domains where a Ni/Mo concentration gradient, instead of a very clear transition
186 between the two domains, should exist. Moreover, according to EDX analysis small amount of
187 Mo^{6+} is also present in the LiNiO_2 domains where some lithium ions have at least one Mo^{6+} as
188 second neighbor. In both cases, new environments with intermediary shifts are created, as shown
189 in the NMR spectra (0-400 ppm in Fig. 3), where several unassigned contributions are detected
190 between the contribution of LiNiO_2 at 680 ppm and the diamagnetic part around 0 ppm. These
191 peaks are referred to as “ $\text{LiNi}_x\text{Mo}_{1-x}$ ” species in Table S8. Based on the area ratios between bulk
192 signal of Li_4MoO_5 and interface signal, we further quantified the Li_4MoO_5 domain sizes to be
193 around 3.2, 4.1, 6.0 and 7.3 nm for $\text{Li}_{1+y}\text{Ni}_{(3-5y)/3}\text{Mo}_{2y/3}\text{O}_2$ ($y=0.03$, 0.06, 0.09, 0.12), respectively,
194 as detailed in Supplementary note I. The domain size of $\text{Li}_{1.09}\text{Ni}_{0.85}\text{Mo}_{0.06}\text{O}_2$ is generally consistent
195 with what we observed from STEM-EDX images in Fig. 2.

196 On the other hand, the detection of peaks on the right-hand side of LiNiO_2 (600-400 ppm),
197 labelled as C and E in Fig.3 and Table S7, seem to indicate lithium ions which have one or two
198 Mo^{6+} in their second coordination sphere and therefore provide more shift than lithium ions at the
199 interface of the diamagnetic domains. Such a behavior concerns 14-20% of all lithium ions, and
200 implies the existence of certain amount of Mo ions doped in the LiNiO_2 phase as proved by TEM-
201 EDX, or there is a slow transition (concentration gradient) between Li_4MoO_5 and LiNiO_2 domains.

202 Combining TEM with NMR results, it is clear that the exact structure of
203 $\text{Li}_{1.09}\text{Ni}_{0.85}\text{Mo}_{0.06}\text{O}_2$ consists of a layered LiNiO_2 -rich phase and a disordered Li_4MoO_5 -rich phase.
204 In this situation, we can now fully understand the intensity reversal of (003) and (104) diffraction
205 peaks in XRD (Fig. 1) because of this layered-disordered intergrowth. We further used a simplified

206 two-phase model ($R\bar{3}m$ $\text{Li}_{1.04}\text{Ni}_{0.93}\text{Mo}_{0.03}\text{O}_2$ and $Fm\bar{3}m$ Li_4MoO_5) to perform the combined
 207 refinement of the collected SXRD and NPD patterns of $\text{Li}_{1.09}\text{Ni}_{0.85}\text{Mo}_{0.06}\text{O}_2$ ($y=0.09$). As shown
 208 in Fig. 1d-e and Table S3, the refinement gave satisfying results, providing a molar ratio of
 209 95.2(7)%:4.8(3)% for the two phases (equivalent to a composition of $\sim\text{Li}_{1.1}\text{Ni}_{0.83}\text{Mo}_{0.07}\text{O}_2$), in good
 210 consistency with the ICP-determined one.



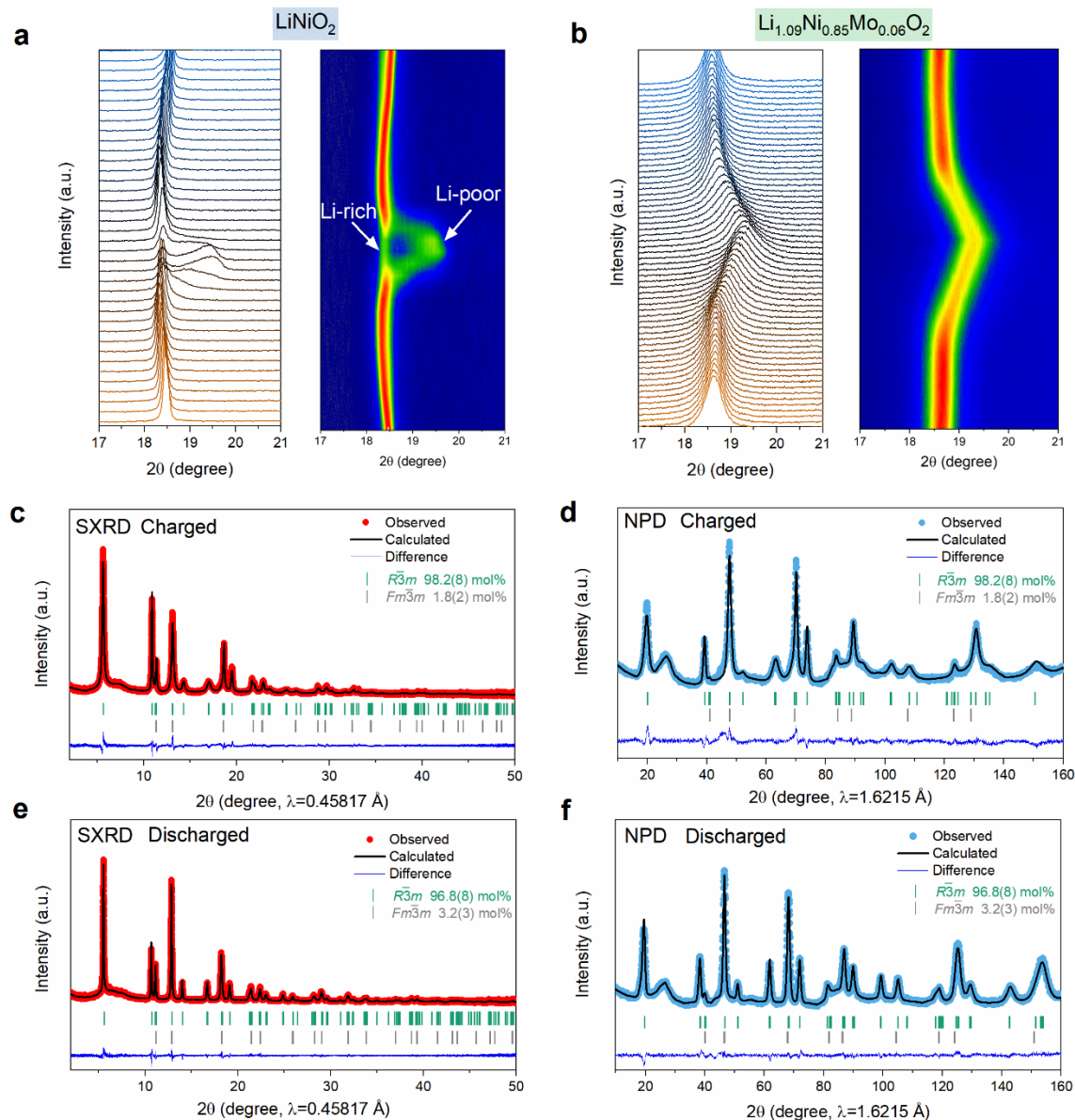
211
 212 **Figure 4. Electrochemistry of $\text{Li}_{1+y}\text{Ni}_{(3-5y)/3}\text{Mo}_{2y/3}\text{O}_2$ ($y=0, 0.03, 0.06, 0.09, 0.12$).** (a) First three cycles of
 213 $\text{Li}_{1+y}\text{Ni}_{(3-5y)/3}\text{Mo}_{2y/3}\text{O}_2$, with their first discharge capacity and first-cycle Coulomb efficiency being noted. (b)
 214 Corresponding dQ/dV plots. (c) Cycling performance of $\text{Li}_{1+y}\text{Ni}_{(3-5y)/3}\text{Mo}_{2y/3}\text{O}_2$. For $y=0.09$ sample, 3 cells
 215 data (in light red) are shown together with average capacity and standard deviation (std.) reported (as shown
 216 by the error bar). (d) Cycling curve of $\text{Li}_{1.09}\text{Ni}_{0.85}\text{Mo}_{0.06}\text{O}_2$ with the dQ/dV plots shown as inset.

217 **Electrochemistry.** A remaining doubt regards if the disordered rock-salt domain is
 218 Li_4MoO_5 -rich phase or $\text{Li}_{1-z}\text{Ni}_{1+z}\text{O}_2$ ($z>0.38$) structure; the latter is well-known to be cation-
 219 disordered due to the similar ionic radius between Li^+ (0.76Å) and Ni^{2+} (0.69Å)^{19,21}. Therefore, one
 220 may consider the possibility of $\text{Li}_{1-z}\text{Ni}_{1+z}\text{O}_2$ formation upon the introduction of lithium-consumable
 221 Mo^{6+} (in forming Li_4MoO_5) that deprives the Li ions in LiNiO_2 . However, this scenario can hardly
 222 happen in our case as we simultaneously put additional Li together with Mo into the structure; as

223 a result, the composition can be written as $\delta\text{LiNiO}_2 \cdot (1-\delta)\text{Li}_4\text{MoO}_5$. Indeed, NMR results even show
224 the decrease of $\text{Li}_{1-z}\text{Ni}_{1+z}\text{O}_2$ species (peak B in Fig. 3) upon the increase of Mo concentration.

225 Besides, the electrochemical response also provides crucial implications on the real
226 structures of these electrodes. As shown in Fig.4a, the electrochemical curves for all the samples
227 show similar wavy characteristics with several small plateaus indicative of typical phase
228 transitions in LiNiO_2 -based compounds. These phase transition behaviors can be more
229 unambiguously observed from the sharp peaks in corresponding dQ/dV profiles in Fig. 4b. One
230 specific feature worth mentioning is the sharpness of these dQ/dV peaks does not evolve too much
231 even with decreasing Ni content. This is in stark contrast to archetypical NMC compounds, in
232 which the Mn/Co substitution in LiNiO_2 dramatically smooths the curves and broadens the dQ/dV
233 peaks.²⁷ This unusual feature matches well with the behavior expected for a two-phase system
234 rather than solid solutions, as the former can largely maintain the LiNiO_2 characteristics even with
235 increasing the Mo content. Therefore, the domain with a disordered rock-salt structure is unlikely
236 to be the $\text{Li}_{1-z}\text{Ni}_{1+z}\text{O}_2$ ($z > 0.38$) phase, as it normally appears with smoother charge/discharge curves
237 due to the “pillar” effect of Ni^{2+} in Li layer that restrains the layer gliding and hence the phase
238 transitions¹⁹.

239 To further validate the analysis above, non-Li-rich Li-Ni-Mo-O phases were also
240 synthesized, namely, $\text{LiNi}_{1-y}\text{Mo}_y\text{O}_2$ ($y=0.02, 0.04, 0.06, \text{ and } 0.08$), for comparison. As shown in
241 Fig. S4a-d, they show similar behavior for the XRD pattern evolution — the ratio of (003)/(104)
242 peak intensity decreases upon increasing the Mo content, though in a severer manner. However,
243 compared to the Li-rich phases, they exhibit smoothed charge-discharge curves with much broader
244 dQ/dV profiles (Fig. S4e-i). This, as has been referred before, implies the formation of a Li_{1-}
245 $z\text{Ni}_{1+z}\text{O}_2$ phase in these non-Li-rich compounds since a large amount of the Li was consumed by
246 forming Li_4MoO_5 . As a result, the non-Li-rich phase shows dramatically decreased capacity once
247 more Mo was added, as the $\text{Li}_{1-z}\text{Ni}_{1+z}\text{O}_2$ phase is unfavorable for Li diffusion. Therefore, these
248 contrasts between Li-rich and non-Li-rich phases further confirm the unique intergrown structure
249 with LiNiO_2 -rich and Li_4MoO_5 -rich (rather than $\text{Li}_{1-z}\text{Ni}_{1+z}\text{O}_2$) domains for the $\text{Li}_{1+y}\text{Ni}_{(3-}$
250 $5y)/3\text{Mo}_{2y/3}\text{O}_2$ samples. It can also be inferred that the extra Li added for Li-rich compositions are
251 mostly electrochemically active or entered into $\text{Li}_{1-z}\text{Ni}_{1+z}\text{O}_2$ lattice to form more electrochemically
252 active LiNiO_2 domain, rather than stay on the particles surface as Li residues.



253

254 **Figure 5. Intra-structural change during cycling.** (a)(b) *In situ* XRD pattern (17-21°) for LiNiO₂ and
 255 Li_{1.09}Ni_{0.85}Mo_{0.06}O₂, respectively, during the H₂→H₃ phase transition. For each compound, left side shows
 256 the patterns evolution while correspondingly, the right side shows the contour plots. Note that the peak shift
 257 looks in a less magnitude in Li_{1.09}Ni_{0.85}Mo_{0.06}O₂ compared with that of LiNiO₂ simply because of the
 258 bifurcation in the latter enables more shift of Li-poor phase. (c)(d) Combined SXR D and NPD refinement
 259 results for Li_{1.09}Ni_{0.85}Mo_{0.06}O₂ charged to 4.3 V. (e)(f) Combined SXR D and NPD refinement results for
 260 Li_{1.09}Ni_{0.85}Mo_{0.06}O₂ discharged to 2.0 V.

261 The benefits of such “Li-rich Ni-rich” combination can be well manifested by the improved
 262 electrochemical performances. With increasing Li and Mo contents, the first-cycle Coulombic
 263 efficiency increases from 91% to around 98%, with the capacity decreasing first and then
 264 increasing to reach even higher values (>220 mA h g⁻¹) at lower Ni content of 85% and 80% (Fig.

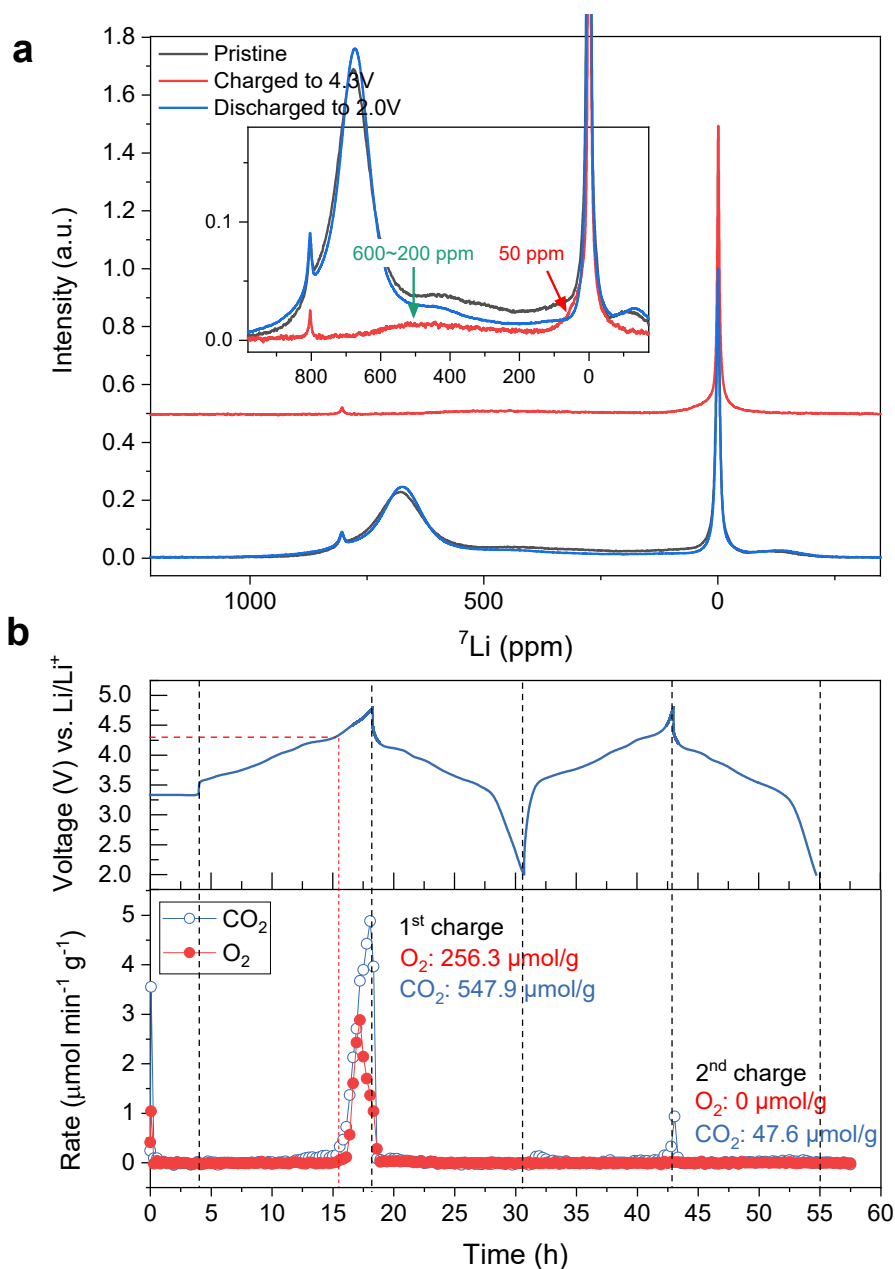
265 4a). Besides, the $y=0.09$ member $\text{Li}_{1.09}\text{Ni}_{0.85}\text{Mo}_{0.06}\text{O}_2$ shows an excellent capacity retention ($\sim 91\%$)
266 after cycling at 0.1C (20 mA g^{-1}) for 100 cycles at room temperature (Fig. 4c) in stark contrast to
267 that of pure LiNiO_2 ($\sim 64\%$). An 80% capacity retention can also be achieved for
268 $\text{Li}_{1.09}\text{Ni}_{0.85}\text{Mo}_{0.06}\text{O}_2$ cycled at 1C (200 mA g^{-1}) for 260 cycles in a half cell versus Li, while in a
269 full cell versus graphite it can sustain for 350 cycles at 0.5C with 87% retention (Fig. S5). It also
270 shows quite stable cycling curves with negligible voltage decay, as observed from both the
271 galvanostatic cycling and dQ/dV profiles in Fig. 4d. Notably, the plateau of the H2-to-H3 phase
272 transition (shaded region in Fig. 4d), which is known for its detrimental effect to the layered
273 structure, was retained very well upon cycling (Fig. 4d). Besides, while the addition of Li and Mo
274 is supposed to downgrade the electronic conductivity of the compounds, $\text{Li}_{1.09}\text{Ni}_{0.85}\text{Mo}_{0.06}\text{O}_2$
275 shows even slightly better rate performance than that of LiNiO_2 (Fig. S6), seemingly resulting from
276 the smaller LiNiO_2 -rich domains/particles with shorter Li diffusion paths. Moreover, the
277 electrochemical performance of $\text{Li}_{1.09}\text{Ni}_{0.85}\text{Mo}_{0.06}\text{O}_2$ was further investigated in a wider
278 electrochemical window (2.0-4.8V) to pursue higher capacity. Figure S7a indicates that an initial
279 capacity of 250 mA h g^{-1} can be obtained at C/10. Though the capacity fades more quickly, it
280 shows a small voltage hysteresis (energy efficiency: 91%) and negligible voltage decay (Fig. S7b-
281 d), which is far more superior to typical Li-rich NMC cathodes.

282 Besides, differential scanning calorimetry (DSC) experiments were performed to evaluate
283 the thermal stability of this new family of electrodes (Fig. S8). Two distinctions can be observed
284 between bare LiNiO_2 and $\text{Li}_{1+y}\text{Ni}_{(3-5y)/3}\text{Mo}_{2y/3}\text{O}_2$ ($y=0.09$ and 0.12) samples. First, the main heat
285 flow peak at around 210°C is very sharp and strong for LiNiO_2 , but is much suppressed for Mo-
286 containing samples (Fig. S8). This difference corresponds well to the structural stability
287 improvement of $\text{Li}_{1+y}\text{Ni}_{(3-5y)/3}\text{Mo}_{2y/3}\text{O}_2$ enabled by the intergrown Li_4MoO_5 -rich domains, which
288 might restrain the structural transformation at high temperature and hence the suppressed heat flow.
289 Second, there are additional weak heat flow peaks below 200°C in $\text{Li}_{1+y}\text{Ni}_{(3-5y)/3}\text{Mo}_{2y/3}\text{O}_2$ samples
290 but are absent in LiNiO_2 . Two possibilities can explain these small peaks. One is due to the anionic
291 redox (as will be shown later) aroused in $\text{Li}_{1+y}\text{Ni}_{(3-5y)/3}\text{Mo}_{2y/3}\text{O}_2$ that produces more reactive species
292 at high voltage and temperature; second is Mo dissolution might be enhanced at elevated
293 temperature. Both possibilities can be reasonable since, with higher Mo content, the heat release
294 below 200°C is even increased (Fig. S8), consistent with more anionic redox contribution or more
295 Mo dissolution triggered in high Mo-content sample.

296 Further shortcomings of these new class of materials in terms of electrochemical
297 performance should be subjected to discussion. One issue is that $\text{Li}_{1.09}\text{Ni}_{0.85}\text{Mo}_{0.06}\text{O}_2$ shows large
298 voltage hysteresis below 3V (Fig.4a) possibly associated with oxygen redox, as discussed later.
299 Though, the energy efficiency can reach $\sim 95\%$ after initial cycles (Fig. S9), acceptable for practical
300 application. Besides, a lower cutoff voltage down to 2.0V was used for achieving high capacities.
301 However, even by cycling the electrode in 2.7-4.3V vs Li, the voltage window typically employed
302 for Ni-rich materials, a capacity up to 210 mA h g^{-1} can also be obtained with good cycling stability
303 (Fig. S10). Moreover, while limitation do exists for $\text{Li}_{1.09}\text{Ni}_{0.85}\text{Mo}_{0.06}\text{O}_2$ when using a high loading
304 (95% active materials, $10\text{-}12 \text{ mg cm}^{-2}$) compared with low loading (80% active material, $6\text{-}8 \text{ mg}$
305 cm^{-2}) as shown in Fig.S11, the performance is highly promising for practical application especially
306 considering it is Co-free.

307 **Structural change.** Since the main active phase in the intergrown structure is LiNiO_2 -rich
308 domain that bears high similarity with pure LiNiO_2 as learnt from TEM, NMR, and
309 electrochemical studies, yet a question lingers why the former shows outstanding electrochemical
310 stability that can hardly be achieved for the latter. First, *in situ* XRD was used to investigate their
311 phase transition behavior during cycling. As shown in Fig. S12a, during the charge process of
312 LiNiO_2 , the (003) diffraction peak undergoes mild changes before reaching 4.2 V. However, once
313 reaching the 4.2 V plateau corresponding to the so-called “H2→H3” phase transition, the (003)
314 peak largely shifts towards higher angle (more than 1°), indicative of a large layer spacing
315 shrinkage. Such a “H2→H3” phase transition is also accompanied by a very large local micro-
316 strain as clearly observed from the very asymmetrical peak at the end of charge (Fig. S12c).
317 Besides, in the second cycle, a bifurcation of the (003) peak emerges due to the co-existence of
318 two phases: the Li-rich and Li-poor phases (Fig.5a and Fig. S12c). This phenomenon, previously
319 called as “bulk fatigue” due to the formation of surface disordered rock-salt phase that causes
320 mechanical failure²⁶, is characteristic of some inactive Li ions (in Li-rich phase) that are not
321 electrochemically accessible, hence the fading of the capacity. We also confirmed that this
322 bifurcation behavior happens similarly for regularly synthesized LiNiO_2 (BASF) in the 2nd cycle
323 but in lesser extent, while it largely aggravates in the 3rd cycle (Fig. S12). By contrast, the (003)
324 peak in $\text{Li}_{1.09}\text{Ni}_{0.85}\text{Mo}_{0.06}\text{O}_2$ shows less shift and less asymmetry during the “H2→H3” phase
325 transition (Fig. S12b). Specially, unlike the case of LiNiO_2 , the (003) peak of $\text{Li}_{1.09}\text{Ni}_{0.85}\text{Mo}_{0.06}\text{O}_2$
326 remains single in the whole “H2→H3” phase transition process (Fig. 5b and Fig.S12d) without

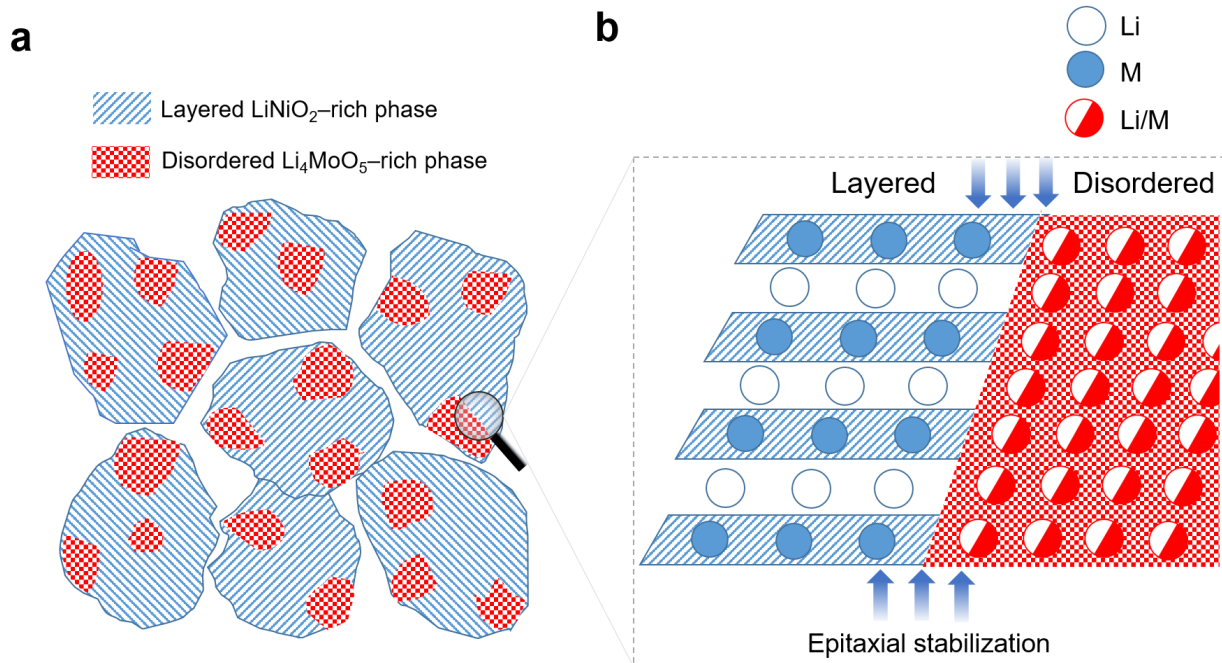
327 any bifurcation. This implies an excellent mechanical reversibility and sustainability of
 328 $\text{Li}_{1.09}\text{Ni}_{0.85}\text{Mo}_{0.06}\text{O}_2$ against LiNiO_2 , thereby explaining the huge electrochemical stability contrast
 329 between these two compounds.



330
 331 **Figure 6. NMR and OEMS study during the cycling of $\text{Li}_{1.09}\text{Ni}_{0.85}\text{Mo}_{0.06}\text{O}_2$.** (a) ^7Li MAS-NMR spectra
 332 of pristine (black), charged (red, top), discharged (blue) $\text{Li}_{1.09}\text{Ni}_{0.85}\text{Mo}_{0.06}\text{O}_2$. Assuming the molybdenum-
 333 rich phase is not active electrochemically, we normalized ^7Li the spectra with respect to the corresponding
 334 peak height at 0 ppm. The inset shows the enlarged view of the overlapped NMR spectra of all three samples.
 335 (b) OEMS result during the first two cycles. A red dashed line marks an onset potential of slightly above
 336 4.3V for oxygen release at the first cycle. The amounts of O_2 and CO_2 release are indicated. CO_2 release is
 337 generally caused by electrolyte oxidation as previously reported²⁸ and further thoroughly discussed in
 338 Supplementary note II.

339 To further examine the intra-cycle structural change, we performed SXRD, NPD, and TEM
340 analysis during the first cycle. The SXRD and NPD patterns of $\text{Li}_{1.09}\text{Ni}_{0.85}\text{Mo}_{0.06}\text{O}_2$ in the charged
341 (4.3 V) and discharged (2.0 V) states were collected and analyzed with Rietveld refinement, as
342 shown in Fig. 5c-f and Table S4-5. The results demonstrate that the long-range cation ordering in
343 $\text{Li}_{1.09}\text{Ni}_{0.85}\text{Mo}_{0.06}\text{O}_2$ is not significantly affected upon cycling, except that a slight deviation of the
344 molar percentage of the Li_4MoO_5 phase is obtained in charged state but which is within the
345 accuracy of quantitative phase analysis by Rietveld method especially considering that the peaks
346 are fully overlapped. Absence of cation migration is also obvious from the HAADF-STEM images
347 of $\text{Li}_{1.09}\text{Ni}_{0.85}\text{Mo}_{0.06}\text{O}_2$ in the charged and discharged states (Fig. S14). The corresponding ED
348 patterns (insets in Fig. S14) indicate the twinned layered O_3 structure is well retained. To further
349 inspect if local structural variation exists, we collected ^7Li MAS-NMR spectra during the first
350 cycle, as shown in Fig. 6a. Interestingly, we find that, after charge, lithium ions are mostly found
351 in diamagnetic environments (i.e. those that are close to Mo^{6+} ions), except for a very broad
352 component between 600 and 200 ppm (Fig.6a inset, green arrow), and a peak at around 50 ppm
353 (Fig. 6a inset, red arrow) which may be assigned to lithium ions at the interface of the
354 molybdenum-rich phase. After discharge, the LiNiO_2 peak almost fully reemerges except for being
355 slightly sharper, accompanied by a subtle intensity decrease in the range of 20-500 ppm (i.e. Li^+
356 ions that are close to Mo^{6+}). These results demonstrate that almost all the Li^+ from LiNiO_2 domain
357 can be removed and can reversibly come back whereas the Li ions in Li_4MoO_5 domains are less
358 active. Such good reversible Li intercalation chemistry in LiNiO_2 domain is in line with the high
359 Columbic efficiency observed in $\text{Li}_{1.09}\text{Ni}_{0.85}\text{Mo}_{0.06}\text{O}_2$, hence explaining its comparable capacity
360 with pure LiNiO_2 even with barely active Li_4MoO_5 domains in the former. Besides, the online
361 electrochemical mass spectrometry (OEMS) experiment (Fig. 6b) shows an onset potential for
362 oxygen release slightly above 4.3 V at the 1st charge, whereas it is totally absent during the second
363 charge, similar to the previous reports on $\text{LiNi}_{0.8}\text{Co}_{0.1}\text{Mn}_{0.1}\text{O}_2$ ²⁸. Thus, good cycling stability is
364 achieved by cutting off the voltage at 4.3 V, while it severely deteriorates when cycled up to 4.8
365 V (Fig. S7a). A SXRD pattern was also collected after cycling the sample for 50th cycles in the 2.0
366 - 4.3 V range (Fig. S15), showing excellent retaining of the original structure without noticeable
367 structural disordering, as deduced from the Rietveld refinement (Table S6).

368
369



370

371 **Figure 7.** Schematic of the layered-disordered intergrowth of “Li-rich Ni-rich” cathode. **(a)** Schematic of
 372 the domains of layered LiNiO_2 -rich phase and disordered Li_4MoO_5 -rich phase in the grains of cathodes. **(b)**
 373 “Epitaxial stabilization” effect of the intergrowth in reinforcing the mechanical and structural stability of
 374 layered phase in the intergrowth structure.

375 The above these results collectively confirm the benefit of such two-phase intergrowth,
 376 with a Li_4MoO_5 domain sizes in the 5-20 nm range, to the structural and mechanical stability of
 377 Ni-rich oxide due to the “epitaxial stabilization” effect, as schematically shown in Fig. 7. The
 378 superimposition of the diffraction peaks (Fig. 1) of the two phases indicates the similar sub-lattice
 379 parameters and hence the coherent epitaxial interface in between the two domains (Fig. 7). As a
 380 result, the mechanical strain energy during (de)lithiation of LiNiO_2 -rich phase can be largely
 381 counteracted by the epitaxial energy from Li_4MoO_5 domains, thereby decreasing the deformation
 382 and improving the cracking resistance. To simulate such effects, a calculation of free energy of the
 383 two intergrowing crystal with a coherent epitaxial interface is indeed possible with the DFT-based
 384 methods, but it requires precisely known atomic structure and chemical composition at the
 385 interface which we did not investigate in detail in this work. Without these prerequisites, the
 386 simulation results will be too speculative being based on extensive assumptions not supported by
 387 the experimental data. In our interpretation of the role of epitaxial stabilization, we refer to very
 388 recent experimental results demonstrating that epitaxial intergrowth of the layered oxide cathode
 389 material with the disordered RS-type phase helps alleviating strain during charge/discharge and
 390 greatly improve the capacity retention^{29,30}. In addition, by checking further the redox mechanism

391 of $\text{Li}_{1.09}\text{Ni}_{0.85}\text{Mo}_{0.06}\text{O}_2$ via XAS complemented by GITT analysis (Fig. S16), we identified a main
392 Ni redox with a bit contribution from O redox triggered by the slight excess Li in LiNiO_2 -rich
393 phase. A typical signature of anionic redox in this system is the large voltage hysteresis observed
394 below 3 V, which aggravates with increasing Li and Mo contents. Such minor O redox contribution
395 may also plays an role on the cycling stability by buffering the electron depletion of O 2*p* states
396 from Ni(3*d*)-O(2*p*) σ -type interactions, as we have envisaged at the beginning.

397

398 **Discussion.**

399 We have explored here a material design strategy by combining the “Li-rich” with the “Ni-
400 rich” concepts together, as shown by the $\text{Li}_{1+y}\text{Ni}_{(3-5y)/3}\text{Mo}_{2y/3}\text{O}_2$ family as a proof of concept. The
401 materials display an intergrowth of a layered LiNiO_2 -rich phase and a disordered Li_4MoO_5 -based
402 domain at the 10 nm scale rather than solid solutions. Such intergrowth of two phases, together
403 with the minor O redox contribution, enables excellent mechanical, structural and cycling
404 stabilities for LiNiO_2 -rich phase, thus expanding the boundary of materials design for practical
405 high-energy-density electrodes.

406 The LiNiO_2 - Li_4MoO_5 intergrowth is reminiscent of previous debates on the real structure
407 of Li-rich NMC ($(1-x)\text{Li}_2\text{MnO}_3 \cdot x\text{LiMO}_2$) compounds on whether they are solid solutions or two-
408 phase (Li_2MnO_3 -rich and LiMO_2 -rich phases) co-existence.³¹⁻³⁶ Similarly, while their XRD
409 patterns exhibit a single-phase feature, local fragments of Li_2MnO_3 can be frequently observed by
410 TEM.^{32,35} An agreement seems to have been achieved that Li-rich NMCs can indeed be considered
411 as solid solutions in the long-range scale but also show some short-range ordering of the two phases.
412 Apparently, the structure of this class of $\text{Li}_{1+y}\text{Ni}_{(3-5y)/3}\text{Mo}_{2y/3}\text{O}_2$ compounds bears the same rationale
413 with Li-rich NMC but with some differences. One is that Mo^{6+} is more insoluble than Mn^{4+} in
414 LiMO_2 layered structures due to its higher valence, hence driving the phase separation of Li_4MoO_5
415 domains within the LiNiO_2 phase (Fig. 7a). Another is that Mo^{6+} is in d^0 electronic configuration
416 and is more prone to forming disordered rock-salt phase in a Li-rich environment³⁷. Besides, with
417 a 4.3 V cutoff voltage, the Li_4MoO_5 -rich phase in $\text{Li}_{1+y}\text{Ni}_{(3-5y)/3}\text{Mo}_{2y/3}\text{O}_2$ compounds is not active,
418 as proven by NMR, unlike Li_2MnO_3 domains in Li-rich NMC charged to 4.8 V, which is crucial
419 to trigger anionic redox and tapping into the associated extra capacity³⁸.

420 Indeed, composite electrode design has been proposed by Thackeray's earlier work in
421 Li_2MnO_3 -based compounds. Several combinations, such as "layered-rocksalt", "layered-layered",
422 "layered-spinel" and so on, were shown to have high capacities and good cycling stabilities.^{39,40}
423 Besides, a "layered-rocksalt" intergrown $\text{Li}_{1.2}\text{Ni}_{0.4}\text{Ru}_{0.4}\text{O}_2$ electrode was also reported recently by
424 N. Li et al.²⁹ While these studies share a similar intergrowth structure, our work, mainly based on
425 the "Li-rich Ni-rich" concept, provides a more practical solution for future cathode design. Besides,
426 several pioneering studies must be mentioned, such as those led by J. Dahn, D. Aurbach, and Y.-
427 K. Sun et al.⁴¹⁻⁴⁴, who attempted to dope $\text{Mo}^{6+}/\text{W}^{6+}$ in LiNiO_2 or its derived Ni-rich compounds,
428 with Mo being infused in grain boundary or segregated in near surface region due to its high
429 insolubility. Hence, our study confirms the Mo^{6+} insolubility they observed, yet it also differs by
430 two aspects: First, in our $\text{Li}_{1+y}\text{Ni}_{(3-5y)/3}\text{Mo}_{2y/3}\text{O}_2$ series, homogenous two-phase intergrowth is
431 achieved, rather than infused boundaries, due to our solution-based synthesis for obtaining a
432 atomically homogeneous precursor. Such an homogeneous two-phase distribution can never been
433 achieved with a simple solid-state synthesis even preceded by a co-precipitation step, as the mass
434 diffusion of Mo^{6+} is difficult and Mo is more prone to precipitating in acidic solution, therefore
435 making it impossible to co-precipitate synchronously with Ni in alkaline solution. Second, Li
436 excess is essential to ensure the two-phase structure and the associated performance as already
437 implied by our previous control studies (Fig. S4).

438 Finally, our conceptualization of "Li-rich Ni-rich" compounds can further expand the space
439 of high-energy cathode materials design, since Mo^{6+} can be replaced by other high-valence
440 transition metal or metalloid ions, such as W^{6+} , Te^{6+} , V^{5+} , Nb^{5+} , Sb^{5+} , Ta^{5+} , Ti^{4+} , Mn^{4+} , or Zr^{4+} etc.
441 A preliminary study has been implemented on Ti^{4+} and Nb^{5+} systems as the representatives of
442 tetravalent and pentavalent transition metal ion doping, showing high resemblance to the case of
443 $\text{Li}_{1+y}\text{Ni}_{(3-5y)/3}\text{Mo}_{2y/3}\text{O}_2$ (Fig. S17). Notwithstanding, some practical parameters of these newly
444 designed electrodes remains to be improved, such as the slightly lower tap density ($1.96(3)\text{g}\cdot\text{cm}^{-3}$)
445 due to the smaller particle size. Future works can focus on seeking better, more abundant, high-
446 valence M ions or combinations of those to further enhance the electrode properties. This has to
447 be done by intensively scrutinizing the ternary composition-structure-electrochemistry
448 relationships of these potential "Li-rich Ni-rich" materials. Besides, the impact of the synthetic
449 method on the microstructure at the nanometer scale and their effect on performances of the
450 electrode remains to be further explored in pursuit of higher practicability. On solving these

451 problems, we believe this study will pave a new way to access practical high-energy-density
452 cathodes for Li-ion batteries.

453

454 **Experimental**

455 **Materials synthesis**

456 $\text{Li}_{1+y}\text{Ni}_{(3-5y)/3}\text{Mo}_{2y/3}\text{O}_2$ ($y=0, 0.03, 0.06, 0.09, 0.12$) and $\text{LiNi}_{1-y}\text{Mo}_y\text{O}_2$ ($y=0.02, 0.04, 0.06, 0.8$) were
457 prepared by a solid-state process preceded by a solution step to obtain the precursors. To prepare the
458 precursors, stoichiometric amounts of lithium acetate dihydrate (2% excess, reagent grade, Sigma-Aldrich),
459 nickel(II) acetate tetrahydrate ($\geq 99.0\%$ (KT), Sigma-Aldrich) and $(\text{NH}_4)_6\text{Mo}_7\text{O}_{24}\cdot 4\text{H}_2\text{O}$ (ACS, 81-83% as
460 MoO_3) were dissolved in water or ethanol, followed by drying the solution to form a viscous gel. The gel
461 was then dried at 120°C in air for at least 8 hours, and hand ground before high-temperature annealing at
462 750°C under oxygen flow for 8 hours, followed by reannealing in the same condition (750°C , 8h, O_2 flow).
463 Note that a low amount of target compound (~ 0.5 g) is easier to obtain phase-pure, whereas scaling up will
464 sometimes lead to easily detected impurities (mainly Li_4MoO_5), as observed from XRD.

465 **Electrochemistry**

466 Electrochemical studies were done in 2032-type coin cells unless otherwise specified. 80 wt.% of active
467 materials with 20 wt.% carbon (Super P) were homogeneously mixed together as cathode electrodes. The
468 coin cells were assembled with the cathode powder (with a loading of $6\text{-}8\text{ mg/cm}^2$) countered by a Li foil
469 as the anode, between which two Whatman GF/D borosilicate glass fiber sheets were used as the separator.
470 LP 57 electrolyte (1M LiPF_6 in EC/EMC= 30:70 wt.%) mixed with 2 wt.% vinylene carbonate (VC) was
471 used as electrolyte for cycling between 2.0 and 4.3 V, whereas a LP30 electrolyte (1M LiPF_6 in EC/DMC=
472 50:50 wt.%, E-Lyte) was used for cycling between 2.0 and 4.8 V.

473 **General characterization (ICP, XRD, NPD, SEM and DSC).**

474 The ICP-AES data was collected with a PerkinElmer NexION 2000 ICP mass spectrometer, and the
475 samples were first dissolved with *aqua regia* and then adjusted to appropriate concentrations with deionized
476 water in a volumetric flask before the measurements. XRD patterns were obtained via a laboratory X-ray
477 diffractometer (BRUKER D8 Advance) equipped with a Cu $K\alpha$ radiation source ($\lambda_{K\alpha 1} = 1.54056\text{ \AA}$, $\lambda_{K\alpha 2}$
478 $= 1.54439\text{ \AA}$) and a Lynxeye XE detector. A homemade airtight cell with a beryllium window was used for
479 *in situ* XRD experiments, for which the electrochemistry was ran synchronously with data acquisition.
480 Constant-wavelength NPD data were collected at room temperature on the WOMBAT high intensity
481 neutron powder diffractometers, with the sample sealed under Argon, using a wavelength of 1.6215 \AA . All
482 the Rietveld refinements of the XRD and NPD patterns were done with the FullProf program⁴⁵. SEM images
483 were obtained on an FEI Magellan scanning electron microscope equipped with an Oxford Instruments
484 energy dispersive X-ray spectroscopy (EDX) detector. EDX was carried out using an acceleration voltage
485 of 20 kV. DSC experiments were carried out with a Mettler Toledo TGA/DSC 3+ (LF 1100 °C) equipment
486 at a rate of $5\text{ }^\circ\text{C min}^{-1}$ between 25 and $300\text{ }^\circ\text{C}$ under a constant Ar gas flow. The samples for DSC were
487 charge to 4.3 V and recovered, washed by DMC for three times, and then dried under vacuum. The tests
488 were conducted by soaking the 3~5 mg dried samples into 100 μl LP57 electrolyte and sealed in an
489 aluminum crucible.

490

491 **TEM**

492 Samples for transmission electron microscopy (TEM) were prepared in an Ar-filled glovebox by grinding
493 the powders in an agate mortar in dimethyl carbonate and depositing drops of suspension onto copper TEM
494 grid with holey carbon support layer. The sample was transported to the TEM column by means of a Gatan
495 vacuum transfer holder completely avoiding contact with air and moisture. Electron diffraction (ED)
496 patterns, high angle annular dark field scanning transmission electron microscopy (HAADF-STEM) images
497 and energy-dispersive X-ray (EDX) spectra were collected with a probe-corrected Titan Themis Z electron
498 microscope operated at 200 kV and equipped with a Super-X EDX detector.

499 **OEMS**

500 Freestanding electrodes comprised 70% wt. active materials, 20% wt. carbon (Super P) and 10% PTFE
501 were used. An in-house designed OEMS cell⁴⁶ was used to run the experiment. 150 μ L of LP30 electrolyte,
502 Li foil as anode and 1 piece of GF/D glassfiber separator were used to assemble the half-cell. The
503 quantitative gas evolution data on *m/z* channels of 32 (O_2) and 44 (CO_2) was collected using an *operando*
504 protocol where the cell was rested for 4 h before and 12 h after the full electrochemistry cycle to stabilize
505 the background signal. The OEMS cells were cycled in the 2.0 - 4.8 V range for two cycles at a C/10 rate
506 (20 mA g^{-1}). At least two cells were tested to ensure results reproducibility.

507 **XAS**

508 Ni K-edge and Mo K-edge XAS spectra were collected in transmission mode at ROCK⁴⁷ beamline of the
509 SOLEIL synchrotron facility at Paris, France. A Si(111) channel-cut quick-XAS monochromator with an
510 energy resolution of 0.7 eV at 7 keV was used. The intensity of the monochromatic X-ray beam was
511 measured using three consecutive ionization detectors. For sample preparation, powders (80% active
512 material and 20% carbon super P) were cycled to specific states of charge and then recovered, washed with
513 DMC for three times, and finally dried under reduced pressure. Then the dried powders were mixed with
514 certain amount of cellulose, and pressed as thin pellets. The pellets were sealed carefully into X-ray
515 transparent plastic bags before taking to XAS measurements. The energy calibration was performed using
516 Ni and Mo foils placed between the second and third ionization chambers. All XAS data were processed
517 with the Athena program⁴⁸.

518 **NMR**

519 Solid-state NMR experiments were performed on a 4.7 T Avance III HD Bruker NMR spectrometer (200
520 MHz for 1H , 77.8 MHz for 7Li , 29.4 MHz for 6Li), using a 1.3 mm magic angle spinning (MAS) probe
521 spinning at 62.5 kHz under pure nitrogen gas. Without temperature regulation, the temperature inside the
522 rotor is expected to be around 50°C. All 7Li NMR experiments were recorded with a rotor-synchronized
523 Hahn echo sequence, and the 90° pulse was set to 1.1 μ s and the chemical shift was referenced with liquid
524 7LiCl in water at 0 ppm (corresponding to a 227 kHz B_1 field strength). The T_1 relaxation times were
525 measured using a saturation-recovery experiment, using 20 x 90° pulses separated by a 1 ms delay for
526 saturation. The T_1 behavior was found to be mono-exponential for the left hand side peaks (around 600-
527 850 ppm) and the T_1 values were around 2-5 ms, as expected for 7Li spins close to paramagnetic Ni^{3+} ions.
528 For the diamagnetic part, the T_1 relaxation was found to be multiexponential, with at least two components,
529 a slow relaxing component with T_1 values between 1 and 1.5 seconds, while a fast relaxing component was
530 observed with T_1 values between 5 and 30ms. This is expected as, first, the spinning sideband from the
531 $LiNiO_2$ peak overlaps with the 0 ppm contribution (fitted in red, on the right hand side, around -120 ppm);
532 second, the diamagnetic contribution is made of lithium in molybdenum-rich domains, embedded in the
533 $LiNiO_2$ phase, and therefore, lithium ions close to the interface will display shorter relaxation times.
534 Therefore, all 7Li spectra were recorded using a 5 to 10 s relaxation delays to ensure a proper quantification
535 of the diamagnetic contribution, with at least 1024 transients recorded to ensure a sufficient signal-to-noise
536 ratio. The 6Li Hahn echo experiment was obtained with a 90° pulse of 2.1 μ s duration, and a 50 ms recovery

537 delay was used, allowing for the recovery of the magnetization of the ${}^6\text{Li}$ close to Ni ions. However, the
538 experiment is not quantitative for the slow relaxing ${}^6\text{Li}$ spins in the diamagnetic phase, and 675,504
539 transients were recorded to obtain a good signal-to-noise ratio. The ${}^6\text{Li}$ NMR spectrum was recorded to
540 confirm that not peak was overlapping with the spinning sidebands that are observed in the ${}^7\text{Li}$ spectrum,
541 as shown in Figure S18. The spectra were deconvoluted with dmfit, using the minimum number of
542 necessary Gausso-Lorentzian spinning sideband patterns (5 spinning sidebands maximum) characterized
543 by a Gaussian/Lorentzian ratio, a position (in ppm), a width (in ppm), and an intensity, all of which were
544 fitted by the program.⁴⁹ The spinning sidebands intensities were fitted (no model was used) independently,
545 and the relative weight of each contribution was obtained from the area of the whole spinning sideband
546 pattern. Special care was taken to measure NMR spectra on fresh samples with as little contact as possible
547 with residual moisture in the glovebox or in the NMR spectrometer.
548
549

550 **ACKNOWLEDGMENTS**

551 This research used resources of the Advanced Photon Source, a US Department of Energy (DOE)
552 Office of Science User Facility, operated for the DOE Office of Science by Argonne National
553 Laboratory under Contract No. DE-AC02-06CH11357. We are grateful to Tuncay Koç for his kind
554 help in performing SEM and EDX measurements, to Valentin Meunier and Ivette Aguilar for their
555 kind help in measuring ICP, to Antonella Iadecola for her help in collecting the XAS spectra, and
556 to Sathiya Mariyappan for her kind help in performing the DSC measurements. A.M.A. is grateful
557 to the Russian Science Foundation for financial support (grant 20-13-00233). Access to TEM
558 facilities was granted by the Advance Imaging Core Facility of Skoltech. J.-M.T and B.L.
559 acknowledge funding from the European Research Council (ERC) (FP/2014)/ERC Grant-Project
560 670116-ARPEMA.

561

562 **AUTHOR CONTRIBUTIONS**

563 B.L. and J.-M.T. conceived the idea and designed the experiments. B.L. carried out the synthesis,
564 structural characterization and electrochemical analysis. G.R. did the analysis of SXRD and NPD
565 data. M.A. collected the NPD patterns. A.M.A. performed TEM experiments and did the analysis.
566 L.Z. did the OEMS experiments and data analysis. M.D. collected NMR data and did the analysis.
567 B.L. and J.-M.T. wrote the manuscript with the contributions from all the authors.

568

569 **DECLARATION OF INTERESTS**

570 The “Li-rich Ni-rich” materials are patented by Collège de France and Umicore (inventors B.L.
571 and J.-M.T.) with patent application numbers being confidential at this stage.

572
573

574 REFERENCES

- 575
576 1. IEA (2020), Global EV Outlook 2020, IEA, Paris [https://www.iea.org/reports/global-ev-outlook-](https://www.iea.org/reports/global-ev-outlook-2020)
577 [2020](https://www.iea.org/reports/global-ev-outlook-2020).
- 578 2. M. S. Whittingham, *Chemical Reviews*, 2004, **104**, 4271-4302.
- 579 3. P. Rozier and J. M. Tarascon, *Journal of The Electrochemical Society*, 2015, **162**, A2490-A2499.
- 580 4. G. Assat and J.-M. Tarascon, *Nature Energy*, 2018, **3**, 373-386.
- 581 5. B. Li and D. Xia, *Advanced materials*, 2017, **29**.
- 582 6. M. Zhang, D. A. Kitchaev, Z. Lebens-Higgins, J. Vinckeviciute, M. Zuba, P. J. Reeves, C. P. Grey,
583 M. S. Whittingham, L. F. J. Piper, A. Van der Ven and Y. S. Meng, *Nature Reviews Materials*,
584 2022.
- 585 7. M. Li, T. Liu, X. Bi, Z. Chen, K. Amine, C. Zhong and J. Lu, *Chem Soc Rev*, 2020, **49**, 1688-1705.
- 586 8. B. Li and J.-M. Tarascon, 2022.
- 587 9. S.-T. Myung, F. Maglia, K.-J. Park, C. S. Yoon, P. Lamp, S.-J. Kim and Y.-K. Sun, *ACS Energy*
588 *Letters*, 2017, **2**, 196-223.
- 589 10. W. Li, E. M. Erickson and A. Manthiram, *Nature Energy*, 2020, **5**, 26-34.
- 590 11. S. S. Zhang, *Energy Storage Materials*, 2020, **24**, 247-254.
- 591 12. J. Liu, Z. Du, X. Wang, S. Tan, X. Wu, L. Geng, B. Song, P.-H. Chien, S. M. Everett and E. Hu,
592 *Energy & Environmental Science*, 2021.
- 593 13. A. O. Kondrakov, H. Geßwein, K. Galdina, L. de Biasi, V. Meded, E. O. Filatova, G. Schumacher,
594 W. Wenzel, P. Hartmann, T. Brezesinski and J. Janek, *The Journal of Physical Chemistry C*, 2017,
595 **121**, 24381-24388.
- 596 14. M. Dixit, B. Markovsky, F. Schipper, D. Aurbach and D. T. Major, *The Journal of Physical*
597 *Chemistry C*, 2017, **121**, 22628-22636.
- 598 15. H. H. Sun, U.-H. Kim, J.-H. Park, S.-W. Park, D.-H. Seo, A. Heller, C. B. Mullins, C. S. Yoon and
599 Y.-K. Sun, *Nature Communications*, 2021, **12**, 6552.
- 600 16. C.-H. Jung, Q. Li, D.-H. Kim, D. Eum, D. Ko, J. Choi, J. Lee, K.-H. Kim, K. Kang, W. Yang and
601 S.-H. Hong, *Journal of Materials Chemistry A*, 2021, **9**, 17415-17424.
- 602 17. C. Zhang, J. Wan, Y. Li, S. Zheng, K. Zhou, D. Wang, D. Wang, C. Hong, Z. Gong and Y. Yang,
603 *Journal of Materials Chemistry A*, 2020, **8**, 6893-6901.
- 604 18. T. P. Dadze, G. A. Kashirtseva, M. P. Novikov and A. V. Plyasunov, *Fluid Phase Equilibria*, 2017,
605 **440**, 64-76.
- 606 19. M. Bianchini, M. Roca-Ayats, P. Hartmann, T. Brezesinski and J. Janek, *Angewandte Chemie*,
607 2019, **58**, 10434-10458.
- 608 20. C. Marichal, J. Hirschinger, P. Granger, M. Menetrier, A. Rougier and C. Delmas, *Inorganic*
609 *Chemistry*, 1995, **34**, 1773-1778.
- 610 21. C. Chazel, M. Ménétrier, L. Croguennec and C. Delmas, *Magnetic Resonance in Chemistry*, 2005,
611 **43**, 849-857.
- 612 22. D. Carlier, M. Ménétrier, C. P. Grey, C. Delmas and G. Ceder, *Physical Review B*, 2003, **67**, 174103.
- 613 23. D. Zeng, J. Cabana, J. Bréger, W.-S. Yoon and C. P. Grey, *Chemistry of Materials*, 2007, **19**, 6277-
614 6289.
- 615 24. C. Chazel, M. Ménétrier, L. Croguennec and C. Delmas, *Inorganic Chemistry*, 2006, **45**, 1184-
616 1191.
- 617 25. H. Li, W. Hua, X. Liu-Théato, Q. Fu, M. Desmau, A. Missyul, M. Knapp, H. Ehrenberg and S.
618 Indris, *Chemistry of Materials*, 2021, **33**, 9546-9559.

- 619 26. C. Xu, K. Marker, J. Lee, A. Mahadevegowda, P. J. Reeves, S. J. Day, M. F. Groh, S. P. Emge, C.
620 Ducati, B. Layla Mehdi, C. C. Tang and C. P. Grey, *Nature materials*, 2021, **20**, 84-92.
- 621 27. N. Zhang, J. Li, H. Li, A. Liu, Q. Huang, L. Ma, Y. Li and J. R. Dahn, *Chemistry of Materials*,
622 2018, **30**, 8852-8860.
- 623 28. D. Streich, C. Erk, A. Guéguen, P. Müller, F.-F. Chesneau and E. J. Berg, *The Journal of Physical
624 Chemistry C*, 2017, **121**, 13481-13486.
- 625 29. N. Li, M. Sun, W. H. Kan, Z. Zhuo, S. Hwang, S. E. Renfrew, M. Avdeev, A. Huq, B. D.
626 McCloskey, D. Su, W. Yang and W. Tong, *Nature Communications*, 2021, **12**, 2348.
- 627 30. D. P. Singh, Y. A. Birkhölzer, D. M. Cunha, T. Dubbelink, S. Huang, T. A. Hendriks, C. Lievens
628 and M. Huijben, *ACS Applied Energy Materials*, 2021, **4**, 5024-5033.
- 629 31. H. Yu, R. Ishikawa, Y. G. So, N. Shibata, T. Kudo, H. Zhou and Y. Ikuhara, *Angewandte Chemie*,
630 2013, **52**, 5969-5973.
- 631 32. Z. Lu, L. Y. Beaulieu, R. A. Donaberger, C. L. Thomas and J. R. Dahn, *Journal of The
632 Electrochemical Society*, 2002, **149**, A778.
- 633 33. K. A. Jarvis, Z. Deng, L. F. Allard, A. Manthiram and P. J. Ferreira, *Chemistry of Materials*, 2011,
634 **23**, 3614-3621.
- 635 34. S. H. Kang, P. Kempgens, S. Greenbaum, A. J. Kropf, K. Amine and M. M. Thackeray, *Journal of
636 Materials Chemistry*, 2007, **17**, 2069-2077.
- 637 35. C. H. Lei, J. Bareño, J. G. Wen, I. Petrov, S. H. Kang and D. P. Abraham, *Journal of Power Sources*,
638 2008, **178**, 422-433.
- 639 36. D. Mohanty, A. Huq, E. A. Payzant, A. S. Sefat, J. Li, D. P. Abraham, D. L. Wood and C. Daniel,
640 *Chemistry of Materials*, 2013, **25**, 4064-4070.
- 641 37. A. Urban, A. Abdellahi, S. Dacek, N. Artrith and G. Ceder, *Phys Rev Lett*, 2017, **119**, 176402.
- 642 38. G. Assat, D. Foix, C. Delacourt, A. Iadecola, R. Dedryvere and J. M. Tarascon, *Nat Commun*, 2017,
643 **8**, 2219.
- 644 39. J. R. Croy, S. H. Kang, M. Balasubramanian and M. M. Thackeray, *Electrochemistry
645 Communications*, 2011, **13**, 1063-1066.
- 646 40. M. M. Thackeray, C. S. Johnson, J. T. Vaughey, N. Li and S. A. Hackney, *Journal of Materials
647 Chemistry*, 2005, **15**, 2257-2267.
- 648 41. U. H. Kim, D. W. Jun, K. J. Park, Q. Zhang, P. Kaghazchi, D. Aurbach, D. T. Major, G. Goobes,
649 M. Dixit, N. Leifer, C. M. Wang, P. Yan, D. Ahn, K. H. Kim, C. S. Yoon and Y. K. Sun, *Energy
650 & Environmental Science*, 2018, **11**, 1271-1279.
- 651 42. C. Geng, D. Rathore, D. Heino, N. Zhang, I. Hamam, N. Zaker, G. A. Botton, R. Omessi, N.
652 Phattharasupakun, T. Bond, C. Yang and J. R. Dahn, *Advanced Energy Materials*, 2021, 2103067.
- 653 43. G.-T. Park, D. R. Yoon, U.-H. Kim, B. Namkoong, J. Lee, M. M. Wang, A. C. Lee, X. W. Gu, W.
654 C. Chueh, C. S. Yoon and Y.-K. Sun, *Energy & Environmental Science*, 2021, **14**, 6616-6626.
- 655 44. D. Rathore, C. Geng, N. Zaker, I. Hamam, Y. Liu, P. Xiao, G. A. Botton, J. Dahn and C. Yang,
656 *Journal of The Electrochemical Society*, 2021, **168**, 120514.
- 657 45. J. Rodriguez-Carvajal, *Physica B: Condensed Matter*, 1993, **192**, 55-69.
- 658 46. L. Zhang, C. Tsolakidou, S. Mariyappan, J.-M. Tarascon and S. Trabesinger, *Energy Storage
659 Materials*, 2021, **42**, 12-21.
- 660 47. V. Briois, C. La Fontaine, S. Belin, L. Barthe, T. Moreno, V. Pinty, A. Carcy, R. Girardot and E.
661 Fonda, *Journal of Physics: Conference Series*, 2016, **712**, 012149.
- 662 48. B. Ravel and M. Newville, *Journal of Synchrotron Radiation*, 2005, **12**, 537-541.
- 663 49. D. Massiot, F. Fayon, M. Capron, I. King, S. Le Calvé, B. Alonso, J.-O. Durand, B. Bujoli, Z. Gan
664 and G. Hoatson, *Magnetic Resonance in Chemistry*, 2002, **40**, 70-76.